INT. J. NUM. METH. HEAT FLUID FLOW, VOL. 3, 545–564 (1993)

FINITE ELEMENT SIMULATION OF THREE-DIMENSIONAL TURBULENT FLOW WITH DECAYING SWIRL

M. R. CASEY, L. KONG AND C. TAYLOR

Department of Civil Engineering, University College of Swansea, Singleton Park, Swansea SA2 8PP, UK

AND

J. O. MEDWELL

Department of Mechanical Engineering, University College of Swansea, Singleton Park, Swansea SA2 8PF, UK

ABSTRACT

A finite element based numerical model is employed to obtain isothermal and heat transfer predictions for the case of turbulent flow with a decaying swirl component in a stationary circular pipe. An assessment is made on the quality of predictions based on the choice of turbulence modelling technique adopted to close the governing equations. In the present work the one-equation, two-equation and algebraic Reynolds stress turbulence models are employed. For the confined flow problem investigated, accurate prediction of the near-wall conditions is essential. This is particularly the case for confined swirling flow where the variation of variables near the wall is often somewhat greater than encountered in pure axial flow. A finite element based near-wall model is employed as an alternative to conventional techniques such as the use of the standard logarithmic functions. Of significance is the fact that flow predictions based on the use of the unidimensional finite element techniques are closer to experiment compared to the wall function based solutions for a given turbulence model. As expected, improvements in the flow predictions directly contribute to improved simulation of the thermal aspects of the problem.

KEY WORDS Decaying swirl Turbulence Near-wall Heat transfer

NOMENCLATURE

C_p	specific heat at constant pressure,	K_a	thermal conductivity of the fluid,
C_1, C_2, C_D	constants employed in the (k–l) and (k–ε) models,	K_c	thermal conductivity of the copper pipe,
C_μ, σ_k, σ_ε		l_M	Prandtl's mixing length,
C_1, α, β, γ	constants employed in the algebraic Reynolds stress model,	l	eddy length scale,
d	internal diameter of the pipe,	l_x, l_y, l_z	direction cosines of a unit normal to the downstream boundary,
e	near-wall function in the algebraic Reynolds stress model,	$\dot{m}$	mass flow rate,
f	function of dimensionless distance in the ARS model,	Nu	Nusselt number,
k	turbulence kinetic energy,	P	production of turbulence kinetic energy,
		$\bar{p}$, p'	mean pressure, fluctuating pressure,

0961–5539/93/060545–20$2.00

Received March 1993

q	heat flux,
R	internal radius of the pipe,
r	radial distance,
$\bar{T}$	mean fluid temperature,
T_b	fluid bulk temperature,
T_w	wall temperature,
ΔT	difference between wall and bulk temperature,
$\bar{u}$, $\bar{v}$, $\bar{w}$	time-averaged velocity components in the x, y and z directions,
u', v', w'	fluctuating velocities in the x, y and z directions respectively,
w^+	dimensionless velocity,
w^*	friction velocity,
w_{mean}	mean axial velocity,
x, y, z	coordinate directions in a Cartesian orthogonal system,
y^+	dimensionless distance measured normal to a boundary,
z/d	dimensionless distance in the axial direction.

Greek symbols

ρ	fluid density,
μ	dynamic viscosity,
ν	kinematic viscosity,
μ_t	turbulent viscosity,
μ_e	effective viscosity ($\mu + \mu_t$),
ε	dissipation of turbulence kinetic energy,
κ	von Kármán's constant,
τ_x, τ_y, τ_z	boundary tractions for the x, y and z mom. equations,
σ	Prandtl's number,
σ_t	turbulent Prandtl number,
τ_w	wall shear stress.

INTRODUCTION

The properties of swirling flows have attracted attention in both an experimental and numerical context for many years. Swirl manifests itself in nature in such forms as whirlwinds and tornadoes. The characteristics of swirling flows have been capitalized in numerous engineering capacities. One example is their employment to promote mixing of fluids ensuring efficient clean combustion in diesel engines, gas turbines and industrial furnaces[1–4]. Heat transfer augmentation due to the presence of a secondary swirling flow has been widely reported, this property is used effectively in turbine blade cooling[5,6].

Despite the widespread experimental interest that swirling flows have generated, their nature and behaviour is still far from understood. Often accurate experimental data are difficult to obtain in confined or complicated geometries. This is particularly true where considerable swirl strength is present provoking such flowfield behaviour as recirculation, increased mixing and vortex breakdown[1]. Due to the considerable expense required to construct innovative prototypes of industrial designs involving swirl, such as combustion chambers and industrial furnaces, a reliable predictive model is attractive both in terms of cost and time scale.

The satisfactory prediction of the flow and heat transfer in a wide range of problems associated with swirl is on-going. Numerical work has been carried out incorporating numerous approaches, examples include the choice of turbulence modelling technique[7], the influence of the boundary conditions[8], the choice of discretization method employed[9] and possible model modification[10]. In recent years, there exists a general progression from the use of simpler turbulence models towards 'higher-order' models incorporating algebraic and differential Reynolds stress closure. These latter models are said to be superior to the conventional 'isotropic' models as they are capable of modelling the history of the turbulent transport using more realistic assumptions, incorporating such effects as the anisotropy of the swirling flowfield[11]. Development and application of these models to flows with swirl is relatively recent, the majority of workers making higher order comparisons with the widely employed (k–ε) model[7,12,13]. In general, improved prediction is reported compared to the use of the (k–ε) model but discrepancies still exist and the higher order models can prove temperamental[7].

Discretization techniques have involved finite difference[12,13], finite volume[7,14] and finite element approaches[9,15]. As far as the authors are aware, the current work represents the only application of the finite element method, involving various turbulence modelling techniques, to

obtain both flow and heat transfer predictions for decaying swirl in a pipe. Few workers have addressed the problem of modelling heat transfer for this case and most of the predictive work carried out has involved analytical techniques[16], numerical approaches typically involve finite difference discretization[17].

One aim of the present work is to assess the quality of the finite element based predictions by varying the turbulence modelling technique. Of equal importance in the assessment of a previously successful[18] finite element near-wall technique as an alternative to conventional methods such as the use of logarithmic laws. Finally, a coupled solid/fluid model is employed to obtain temperature field predictions based on various isothermal solutions.

MATHEMATICAL MODEL

The present work relates to steady-state incompressible turbulent flow within a stationary pipe. In abbreviated form, employing indicial notation, the governing time-averaged Navier–Stokes equations for such a case are given as:

Momentum:
$$\rho\overline{u_j}\frac{\partial\overline{u_i}}{\partial x_j} = -\frac{\partial\bar{p}}{\partial x_i} + \frac{\partial}{\partial x_j}\left[\mu\left(\frac{\partial\overline{u_i}}{\partial x_j} + \frac{\partial\overline{u_j}}{\partial x_i}\right) - \rho\overline{u_i'u_j'}\right] \tag{1}$$

Conservation of mass:
$$\frac{\partial\overline{u_i}}{\partial x_i} = 0 \tag{2}$$

The current investigation is concerned with modelling swirl in a *stationary* pipe, the swirl component having been generated experimentally upstream of the test section, as described later. Therefore, since no external force exists to promote swirl, there are no body forces in the momentum equations. In order to close the governing equations, in a time-averaged form, it is necessary to represent the Reynolds stress tensor, $\rho\overline{u_i'u_j'}$, which contains the fluctuating velocity components. For a three-dimensional problem, this term represents six Reynolds stress components. The representation of these terms, which describe each of the component stresses originating from the turbulence in the fluid, comes under the general heading of turbulence modelling.

Turbulence modelling

Early work in turbulence modelling by Boussinesq[19] involved the assumption that the turbulent stresses were related to the mean velocity gradient via a proportionality factor given by an eddy viscosity (μ_t) which can be represented by:

$$\tau_{ij} = -\rho\overline{u_i'u_j'} = \mu_t\left[\frac{\partial\overline{u_i}}{\partial x_j} + \frac{\partial\overline{u_j}}{\partial x_i}\right] \tag{3}$$

The one equation model of turbulence, or (k–l) model, involves a description of the turbulent viscosity in terms of the root of the turbulence kinetic energy, i.e.:

$$\mu_t = \rho C_\mu k^{1/2} l \tag{4}$$

in which C_μ is a constant and $l = 2.5l_M$, where the length scale l_M is based on the Prandtl mixing length. The mean turbulence kinetic energy, $k = [\overline{u_i'^2}]/2$, reflects the level of turbulent intensity emanating from the fluctuating velocities. In order to represent the diffusive and convective properties present within the flow, the kinetic energy values can be obtained from a transport equation which includes terms which reflect the properties of the flow in a similar manner to the momentum equations. The derivation of the turbulence kinetic energy transport equation involves the manipulation of the Navier–Stokes equations, its full derivation is given in numerous

texts[20]. The resulting kinetic energy equation takes the form:

$$\underbrace{\rho\overline{u_j}\frac{\partial k}{\partial x_j}}_{\text{convection}} = \underbrace{\frac{\partial}{\partial x_j}\left[\left(\mu+\frac{\mu_t}{\sigma_k}\right)\frac{\partial k}{\partial x_j}\right]}_{\text{diffusion}} + \underbrace{\mu_t\frac{\partial \overline{u_i}}{\partial x_j}\left(\frac{\partial \overline{u_i}}{\partial x_j}+\frac{\partial \overline{u_j}}{\partial x_i}\right)}_{\text{generation}} - \underbrace{\rho C_D\frac{k^{3/2}}{l}}_{\text{dissipation}} \tag{5}$$

In order to avoid describing the length scale empirically, a second transport equation has been developed[21]. The two-equation or (k–ε) model of turbulence employs a transport equation in addition to those previously described which represents the dissipation of the turbulence kinetic energy. Its derivation is well documented, the author recommends Thomas[22] for its full derivation and its finite element form. This equation takes the form:

$$\underbrace{\rho\overline{u_j}\frac{\partial \varepsilon}{\partial x_j}}_{\text{convection}} = \underbrace{\frac{\partial}{\partial x_j}\left[\left(\mu+\frac{\mu_t}{\sigma_\varepsilon}\right)\frac{\partial \varepsilon}{\partial x_j}\right]}_{\text{diffusion}} + \underbrace{\rho C_1 C_\mu k\frac{\partial \overline{u_i}}{\partial x_j}\left(\frac{\partial \overline{u_i}}{\partial x_j}+\frac{\partial \overline{u_j}}{\partial x_i}\right)}_{\text{generation}} - \underbrace{\frac{\rho C_2\varepsilon^2}{C_\mu k}}_{\text{dissipation}} \tag{6}$$

The length scale is now determined from the following relationship[21]:

$$l = \frac{k^{3/2}}{\varepsilon} \tag{7}$$

If this relationship is then substituted into (4), the turbulent viscosity is now given as:

$$\mu_t = \rho C_\mu\frac{k^2}{\varepsilon} \tag{8}$$

The following constants were adopted for the present work[22]: $C_D = 0.418$; $C_\mu = 0.22$; $C_1 = 1.43$; $C_1 = 0.18$; $\sigma_k = 1.53$ and $\sigma_\varepsilon = 1.0$. Discrepancies reported between prediction and experiment employing the previously described models are thought to be attributed to the 'eddy viscosity' models which assume isotropic conditions in that a single eddy viscosity formulation is used to calculate all the individual Reynolds stress components. Several workers advocate the use of higher order turbulence modelling techniques in order to capture the true anisotropic nature of flows with swirl[12,13].

In order to fully describe the dissipative, diffusive and redistributive processes of turbulent flows it is possible to derive partial differential equations for each of the Reynolds stresses[23]. In doing so, such effects as a non-isotropic strain field, wall damping influences and streamline curvature can be incorporated. The full form of the Reynolds stress expressions is given in Launder *et al.*[23]. The full form of the stresses have a number of restrictions and simplifications made to them in order to make them more manageable, since the computational power required to solve the full system, particularly in three dimensions, is formidable.

In forming *algebraic* expressions for the stresses, local equilibrium is assumed which implies that the convective and diffusive terms are neglected. Following Launder *et al.* an alternative scalar representation of the decay-rate term is employed which assumes that the dissipative motions are isotropic[23]. By making such assumptions the full Reynolds stress expressions are reduced to the following form:

$$0 = \underbrace{P_{ij}}_{\text{production}} - \underbrace{\frac{2}{3}\delta_{ij}\varepsilon}_{\text{dissipation}} - \underbrace{C_1\frac{\varepsilon}{k}\left(\overline{u_i'u_j'}-\frac{2}{3}\delta_{ij}k\right)-\alpha\left(P_{ij}-\frac{2}{3}\delta_{ij}P\right)}_{\text{pressure–strain}} - \underbrace{\beta\left(D_{ij}-\frac{2}{3}\delta_{ij}P\right)-\gamma\left(\frac{\partial \overline{u_i}}{\partial x_j}+\frac{\partial \overline{u_j}}{\partial x_i}\right)k}_{\text{pressure–strain}} \tag{9}$$

where:

$$P = -\overline{u_i'u_k'}\frac{\partial \overline{u_i}}{\partial x_k} \qquad P_{ij} = \left[-\overline{u_i'u_k'}\frac{\partial \overline{u_j}}{\partial x_k} - \overline{u_j'u_k'}\frac{\partial \overline{u_i}}{\partial x_k}\right]$$

$$D_{ij} = \left[-\overline{u_i'u_l'}\frac{\partial \overline{u_l}}{\partial x_j} - \overline{u_j'u_l'}\frac{\partial \overline{u_l}}{\partial x_i}\right]$$

In (9) the pressure strain term has been recast into a form more generally applied based on reasoning by Launder *et al.*[23] following work by Nato *et al.*[24] and Rotta *et al.*[25]. An assumption is also made with regard to equating the production and dissipation terms which is also consistent with local equilibrium. By doing so P is replaced by ε to form:

$$(1-\alpha)\left[-\overline{u_i'u_l'}\frac{\partial \overline{u_j}}{\partial x_l} - \overline{u_j'u_l'}\frac{\partial \overline{u_i}}{\partial x_l}\right] + \beta\left[\overline{u_i'u_l'}\frac{\partial \overline{u_l}}{\partial x_j} + \overline{u_j'u_l'}\frac{\partial \overline{u_l}}{\partial x_i}\right]$$
$$-\gamma\left(\frac{\partial \overline{u_i}}{\partial x_j} + \frac{\partial \overline{u_j}}{\partial x_i}\right)k - \frac{\varepsilon}{k}\left[C_1\overline{u_i'u_j'} + \frac{2}{3}(1-\alpha-\beta-C_1)\delta_{ij}k\right] = 0 \quad (10)$$

This expression can now be solved for the $\overline{u_i'u_j'}$ stress components appearing in the term $C_i\overline{u_i'u_j'}$. The relations employed for the six Reynolds stress components are given in the Appendix. The expressions given in (21) to (26) are strongly coupled and an iterative procedure is required for their solution. Often further simplifications of the Reynolds stress expressions are made. These include the representation of the primary shear stresses invoking the isotropic eddy viscosity hypothesis or the neglection of the streamwise gradients[26]. Experimental evidence[27] suggests that flow with decaying swirl involves significant streamwise gradients therefore such simplifications were not employed in the current work and the original expressions given in (21) to (26) are retained.

In the Reynolds stress equations the turbulent viscosity is calculated from (8) having obtained k and ε from (5) and (6), respectively. The empirical functions C_1, α, β and γ are given by the following expressions[23]:

$$C_1 = 1.5 - 0.5f, \qquad \alpha = 0.7636 - 0.06f, \qquad \beta = 0.1091 + 0.06f, \qquad \gamma = 0.182 \quad (11)$$

in which f is a function of the dimensionless distance from the wall. The following relationship for f was employed in the current work:

$$f = e\frac{L}{y} \quad (12)$$

Integral formulations have been employed to calculate y to take into account adjacent walls in square ducts[26]. In the current study, for a pipe with a curved boundary, y is taken as the normal distance from the point considered to the pipe wall. The length scale, L, in (12) is given by:

$$L = \frac{k^{3/2}}{\varepsilon} \quad (13)$$

The coefficient e is chosen so that f has a value of unity in the near-wall region where the turbulence is in a state of local equilibrium[26]. For the present work an $e = 2.5$ is employed.

Heat transfer modelling

In formulating the solid/fluid model for convective heat transfer in confined turbulent swirling flow a number of assumptions are made:

- the heat flow is simplified in that convection and conduction are taken into account but both radiation and internal heat generation due to viscous forces are neglected;

- the heat source is assumed to be known either within the pipe or on its outer extremity;
- for the pipe section considered and the temperature ranges encountered, the flow properties are assumed to remain constant.

If constant flow properties are assumed, the heat transfer within a gas under steady state turbulent flow conditions may be written as[28]:

$$\rho C_p \overline{u_i} \frac{\partial \bar{T}}{\partial x_i} = \frac{\partial}{\partial x_i}\left[C_p \left(\frac{\mu}{\sigma} + \frac{\mu_t}{\sigma_t} \right) \frac{\partial \bar{T}}{\partial x_i} \right] \tag{14}$$

in which $\bar{T}$ describes the time-averaged mean fluid temperature, C_p the specific heat of the fluid at constant pressure and σ, σ_t the Prandtl and turbulent Prandtl number of the fluid, respectively. A Boussinesq approximation has been employed in (14) relating the mean and fluctuating temperature fields. In the current study the numerical model takes into account the encompassing solid. The governing equation within the solid, having no convection terms, is represented by:

$$0 = \frac{\partial}{\partial x_i}\left[K_c \frac{\partial \bar{T}}{\partial x_i} \right] \tag{15}$$

where K_c represents the thermal conductivity of the solid. In this case the solid refers to a copper pipe for which a value of $K_c = 386$ W/(m°C) is taken. The Prandtl number, σ, and the turbulent Prandtl number, σ_t are taken to be 0.7 and 0.95 respectively in the fully turbulent region of the pipe ($0 \leqslant y^+ \leqslant 30$)[6]. Due to the changing flow regimes that exist close to the wall due to the damping of the turbulence, the value of σ_t varies. No established formulae exist to represent this variation in the near wall region, particularly for flow with swirl. At present a previous distribution[6], which has been used successfully for the case of swirling flow in a rotating pipe, is employed such that:

$$\begin{aligned}
&y^+ > 25 && \sigma_t = 0.95 \\
&25 \geqslant y^+ > 17 && \sigma_t = 0.95 + 0.45(25 - y^+)/8 \\
&17 \geqslant y^+ > 13 && \sigma_t = 1.4 \\
&13 \geqslant y^+ > 5 && \sigma_t = 1.4 - 0.7(13 - y^+)/8 \\
&y^+ \leqslant 5 && \sigma_t = 0.7
\end{aligned} \tag{16}$$

in which y^+ is defined by the following relationship:

$$y^+ = \frac{y\sqrt{(\tau_w/\rho)}}{\nu} \tag{17}$$

where τ_w represents the wall shear stress and y is measured along the inward normal to the pipe wall.

PROBLEM DESCRIPTION

Extensive experimental data has been recorded[27] on a reproduction of an apparatus originally designed by Sparrow *et al.*[29]. The present study is primarily numerical in nature, therefore only brief experimental details are provided. Air is drawn through the swirl generation device which comprised of a Perspex cylinder with holes drilled tangentially to its surface located upstream of the test section. The resulting swirl was then allowed to decay along the test pipe, of internal diameter 50 mm and length 4 m. The current study is concerned with modelling the decay of the swirl in the downstream region of the test pipe spanning the section between 59 and 71 pipe diameters downstream of the pipe inlet. Letting z represent the distance along the pipe and d the pipe diameter, the section concerned spans $z/d = 59$ to $z/d = 71$. The air flow through the

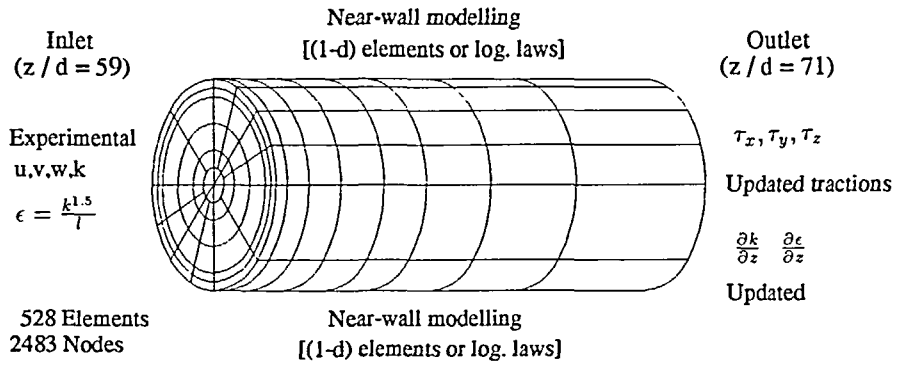

Figure 1 Mesh and boundary conditions for the flow problem

pipe corresponded to a $Re = 20{,}000$, measured by a self-averaging pitot tube downstream of the test section. Hot-wire anemometry was employed to record the mean and fluctuating variables of the flow field. Thermocouples and temperature probes were employed to record the wall and air temperatures. The validity of the experimental data employed in the current work, by comparison with previously published work, is discussed elsewhere[27,30].

Problem boundary conditions

Satisfactory modelling of the isothermal and heat transfer conditions of the flow considered is, in common with practically all numerical simulations, highly dependent on adequate boundary conditions. The finite element mesh and the subsequent boundary conditions employed for the flow investigation are given in *Figure 1*. The main domain of the flow mesh comprises of (3-d) 20-noded tri-quadratic elements, the choice of which is explained elsewhere[18], based upon the application of the Patch test[31]. In order to avoid excessive (3-d) mesh refinement the mesh is terminated a short distance away from the pipe wall where the appropriate near-wall techniques are employed, as described later. The flow boundary conditions employed, as shown in *Figure 1*, can be summarised as:

Inlet: In the numerical modelling of swirl in pipes realistic experimental inlet profiles generally result in improved prediction downstream relative to the specification of 'idealized' profiles[8]. Experimental profiles were imposed at the section inlet ($z/d = 59$) for the velocity and kinetic energy fields. As the dissipation rate, ε, cannot be determined experimentally, the inlet values are assumed to obey the mixing length relation given in (7) in which k refers to the experimental values. A survey of the relevant literature reveals that no definitive length scale formulation has been developed for flow with swirl. In the present work the mixing length at the inlet was assumed to be $l = 0.4y$, where y is the normal distance away from the pipe wall[18].

Outlet: The usual practice at the exit boundary is to assume fully developed conditions by setting axial gradients to zero. In the current study the experimental data indicated that the swirl had not died out completely at $z/d = 71$ and thus the axial gradients differed from zero. It is therefore more realistic and convenient to employ an updated traction technique[30] throughout the numerical procedure. This method ensures compatibility of the numerical values at the outlet nodes with the values at the nodes located immediately upstream.

Wall: For a stationary pipe all the variables are set to zero at the pipe wall.

Near-wall: Two techniques were employed to provide boundary conditions at the edge of the main domain mesh close to the wall. The first involved the use of the standard logarithmic

laws[18], the second involved the use of unidimensional finite element strings[18,30]. The former method was originally developed for fully developed flows and its use in complex flows with swirl has been questioned[13,15]. The latter method has been employed successfully in the past and has found to lead to improved prediction relative to conventional techniques[18].

When using the unidimensional element technique, strings of (1-d) finite elements are employed to solve the governing equations in the near-wall region between the edge of the main domain and the pipe wall. Two unidimensional element techniques were employed. One method employed strings of 3-noded parabolic (1-d) elements normal to the pipe wall as shown in *Figure 2*. The assumption being that variable gradients with respect to the directions parallel to the wall are assumed small compared to variable gradients with respect to the normal direction. Consequently the near-wall governing equations neglect the streamwise (z-direction) variable gradients. In this case unidirectional assumptions are made in a similar manner to the use of the logarithmic laws, the difference being governing equations are solved in the near-wall region as opposed to using empirical functions.

The second unidimensional element technique involves constructing rows of (1-d) elements in both the normal and streamwise directions, as shown in *Figure 3*. These strings were again used to solve the near-wall equations which now include variable gradients in the streamwise direction. This method is more realistic for the case of a decaying swirl in which the streamwise gradients are likely to have a more dominant role in the solution of the near-wall equations. The full procedure adopted in employing (1-d) elements can be found elsewhere[18,30]. In adopting both finite element approaches, *interfacial* nodes are set up which are common to both the 20-noded and (1-d) element meshes. It is at these nodes that the near-wall boundary conditions are applied for the (3-d) mesh. Both the wall function and finite element techniques involve the use of previous iteration values as the solution procedure alternates between the near-wall region and the main domain.

The mesh and boundary conditions employed for the heat transfer problem are given in *Figure 4*. For the heat transfer investigation, three-dimensional 20-noded isoparametric elements were employed over the entire fluid and solid domains. For the current study, involving strongly convective heat transfer, it is necessary to incorporate a fine mesh in the near wall region in order to capture the large temperature gradients which exist. The fine discretization within the near wall zone does not necessarily involve considerable computational expense since the only variable solved for at each node is the temperature. The frontwidth associated with the solution technique is considerably smaller for the heat transfer problem compared to the flow investigation which involves the evaluation of up to four variables per node.

In discretizing the entire solid/fluid domain each finite element relates either to the fluid or the solid. This implies that an interface is set up between adjacent finite elements representing the fluid or the solid. It is necessary to ensure that the continuity of the heat transfer is satisfied over such an interface. The current method ensures this is satisfied by assuming continuity of

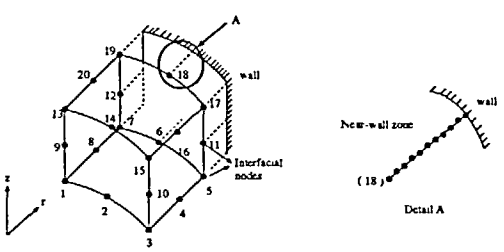

Figure 2 Near-wall unidimensional strings in a direction normal to the wall

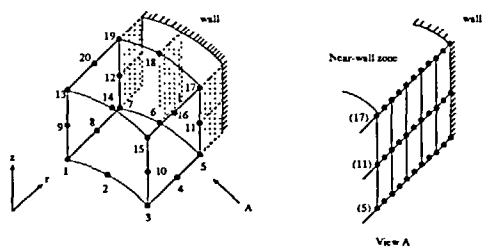

Figure 3 Near-wall unidimensional strings in normal and axial directions

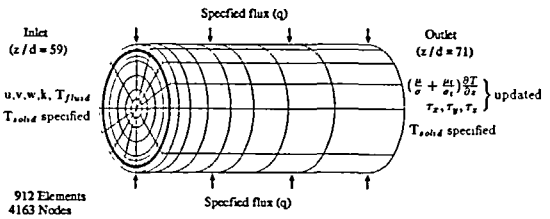

Figure 4 Mesh and boundary conditions for the heat transfer problem

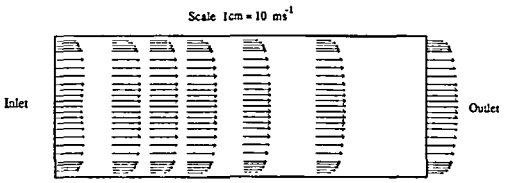

Figure 5 Predicted axial velocity vectors (k–l) model and (1–d) elements

flux along the internal element boundaries such that:

$$\underbrace{\int_\Gamma C_p\left[\frac{\mu}{\sigma}+\frac{\mu_t}{\sigma_t}\right]\frac{\partial \bar{T}}{\partial n}\,\mathrm{d}S}_{\text{fluid}} = \underbrace{\int_\Gamma K_c\frac{\partial \bar{T}}{\partial n}\,\mathrm{d}S}_{\text{solid}} \tag{18}$$

where S relates to an element surface, C_p to the specific heat of the fluid at constant pressure and n refers to the outward normal to the interface. The temperature field is usually determined from the simultaneous solution of the momentum, continuity and energy equations. If the fluid properties are assumed constant for the temperature ranges considered and the convective terms assumed to dominate, the momentum equations can be uncoupled from the energy equation. However, the temperature field is dependent on the velocity distribution via the convection term and is also dependent on the turbulent viscosity distribution in the conduction term of (14). These distributions are obtained from the previously converged flow predictions. An assessment is then made of the effect on heat transfer predictions based on various converged isothermal solutions.

Due to the dependence of temperature on the velocity and viscosity fields, the heat transfer problem necessitated the prescription of velocity and turbulent viscosity values throughout the mesh, including the near wall region, prior to solving for temperature. When employing wall functions the velocity field was calculated based on y^+ (17) values at the near wall zone/main domain interface using empirical formulae. Each of the y^+ values were linearly interpolated from their value at the edge of the near wall zone to the solid wall. When employing a 20-noded mesh in the near wall region for the heat transfer problem, each of the nodes in the near wall region have associated with them a y^+ value which is used to calculate the velocity and turbulent viscosity field using the empirical formulae dependent on y^+. In this way a heat transfer solution is obtained based on a flow solution involving wall functions. Alternatively, nodes within the 20-noded elements of the heat transfer mesh in the near wall region can correspond to nodes making up the unidimensional element strings. In this case the converged values of velocity and turbulent viscosity within the near wall zone are simply assigned to the equivalent nodes in the 20-noded elements.

The complete set of boundary conditions for the heat transfer investigation are given in *Figure 4*. At the section inlet experimental fluid temperature values were imposed together with wall temperature readings. Along the length of the section, on the outer surface of the pipe, an experimentally determined heat flux was applied. At the exit boundary the flux conditions within the fluid domain are unknown and it is convenient to allow the downstream temperatures to develop by updating the flux boundary condition. The flux values within the fluid at the exit, initially guesstimated and subsequently updated, have the form:

$$f_i = \left[\frac{\mu}{\sigma}+\frac{\mu_t}{\sigma_t}\right]\frac{\partial \bar{T}}{\partial x_i}\,l_i \tag{19}$$

where l_i is the component of an unit outward normal to the exit boundary. In this way compatibility is again ensured in this region. In a similar manner to that of the flow investigation it is incorrect in this case to assume fully developed conditions at the section outlet.

RESULTS AND DISCUSSION

Figure 5 illustrates an example of the predicted axial velocity vectors along the pipe section. It is seen that the specified axial velocity profile at $z/d = 59$ has a 'dip' present near the pipe axis. This is in contrast to a typical turbulent fully developed axial velocity profile which usually has a flatter shape and a maximum value located at the pipe axis. As the swirl decays along the pipe, one of the effects on the flow field is to bring about a significant reduction in the radial pressure gradient. This causes a larger positive pressure gradient at the pipe axis to be set up compared to that associated with pure axial flow. This behaviour causes a reduction in the axial velocity value at the axis and, for continuity to be satisfied, results in a shift of the maximum value away from the centreline, hence the 'dip' present in the $z/d = 59$ profile.

In *Figures 6* and *7*, axial velocity comparisons are given at two axial locations, at $z/d = 62$ and at the section outlet, $z/d = 71$. An $r/R = 0.0$ indicates the pipe axis and an $r/R = 1.0$ indicates the pipe wall. Each of the numerical solutions correctly predict the movement of the maximum value towards the pipe axis downstream. The maximum difference between computation and experiment employing the (k–l) model combined with any of the near wall methods was approximately 8%. From *Figure 6* it is seen that the solutions obtained using the unidimensional techniques are slightly closer to the experimental profile compared to the wall function based solution.

In common with the (k–l) model solutions, the (k–ε) and ARS profiles in *Figure 7* show a tendency to overpredict near the pipe axis and underpredict near the pipe wall. This predictive behaviour at the pipe axis employing the (k–ε) model has been reported previously and has been attributed to an overestimation of the diffusive transport of momentum in the radial direction[7]. Khodadadi *et al.*[8] have modelled the data of Weske *et al.*[32] and have reported an overprediction using the (k–ε) model of the order of 25% at the pipe axis. The velocity underprediction near the pipe wall can be attributed to an underestimation of the shear stress.

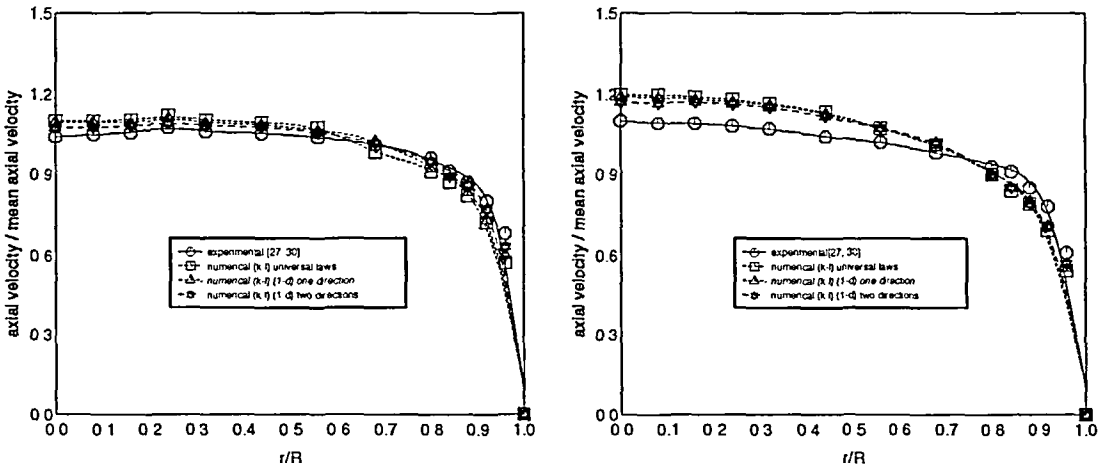

Figure 6 Axial velocity comparison (k–l) model: (a) $z/d = 62$; (b) $z/d = 71$

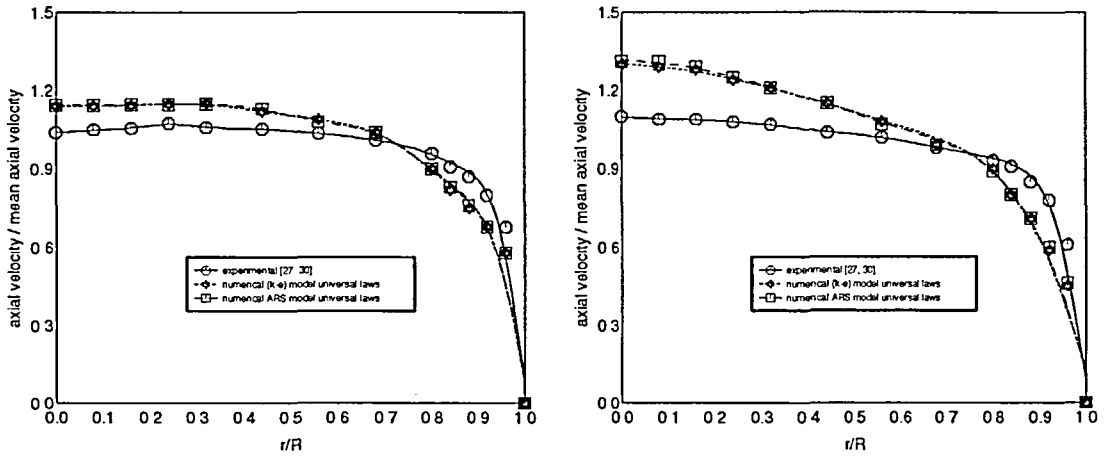

Figure 7 Axial velocity comparison (k–ε), ARS: (a) $z/d=62$; (b) $z/d=71$

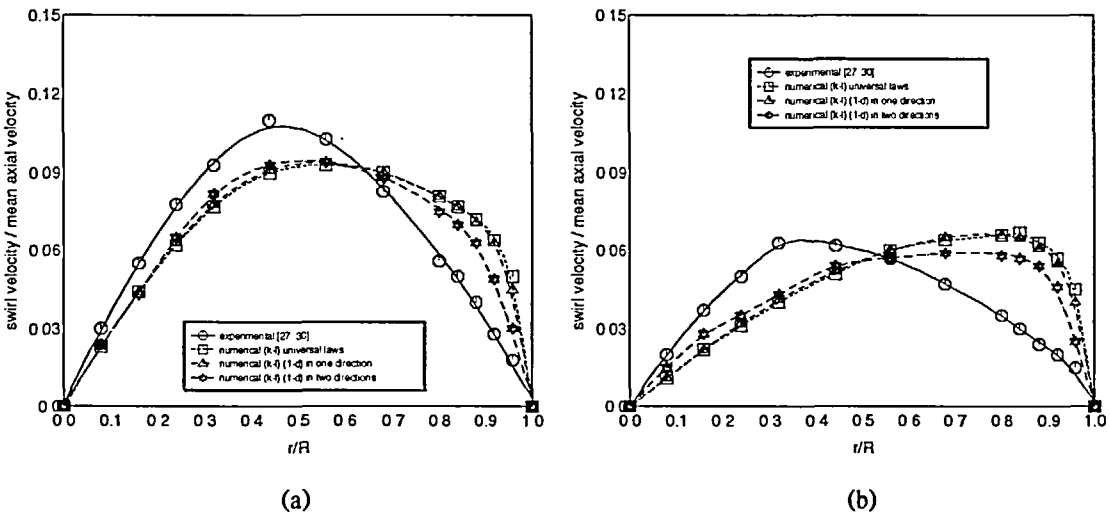

Figure 8 Swirl velocity comparison (k–l) model: (a) $z/d=62$; (b) $z/d=71$

Figures 8 and *9* include the corresponding swirl velocity comparisons. The tangential velocity profile issuing from a swirl generator usually takes the form of a combined free and forced vortex. The boundary between the two is indicated by the location of the maximum tangential velocity. As the tangential velocity has a zero value at the wall (stationary pipe) and at the axis (no flow over an axis of symmetry) the maximum occurs between the wall and the axis. In decaying swirl flow in a pipe, the tangential velocity maximum moves towards the centre of the pipe reducing in size as it decays downstream. For the section of pipe considered, the location of the maximum was found to move experimentally from $r/R = 0.5$ at $z/d = 59$ to $r/R = 0.34$ at $z/d = 71$.

It is apparent from *Figures 8* and *9* that the numerical models incorrectly predict a movement of the maximum towards the pipe wall downstream. This predictive behaviour has also been

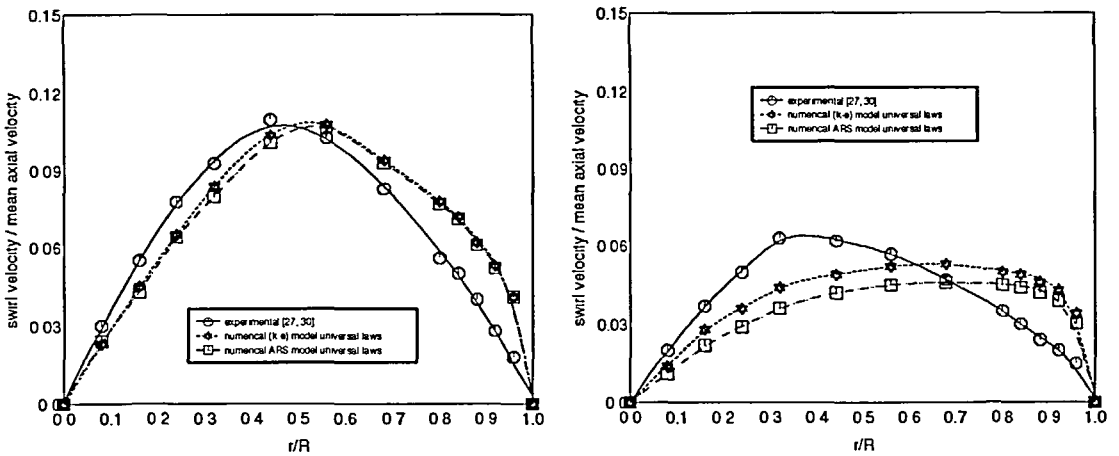

Figure 9 Swirl velocity comparison (k–ε), ARS: (a) $z/d=62$; (b) $z/d=71$

reported previously[8]. As far as the (k–l) model results are concerned, the use of the unidimensional element techniques has resulted in improved prediction relative to the use of the wall functions. The employment of (1-d) elements in two directions to solve the near-wall governing equations improves upon the use of (1-d) elements in one direction in which the streamwise gradients were neglected. This is encouraging as the improvement can be attributed to the more realistic assumptions made in the near wall zone when employing unidimensional elements.

It is seen that there is again similarity in the (k–ε) and ARS model predictions. Other workers[11] have reported such predictive similarity for these models in the 'recovery' region where the swirl component dies out and fully developed conditions are approached. The present study is concerned with a relatively weak swirl component, it is likely that further differences in prediction between these models are likely to come about when modelling flow with a stronger component in which the benefits of employing anisotropic assumptions are highlighted. Of particular interest is the fact that the near-wall (k–l) model and (1-d) in two directions predictions are actually of a lower magnitude and closer to the experimental data than each of the numerical solutions. *Figure 10* gives swirl velocity vector solutions at varying sections downstream using, for example, a one equation model and wall functions. This Figure illustrates the incorrectly predicted increase in magnitude of the vectors near the wall downstream compared to the imposed $z/d = 59$ values.

A number of workers have succeeded in modelling some of the mean flow properties of swirling flows, yet invariably have had difficulty in computing realistic turbulence quantities such as the kinetic energy[8,11,13]. When employing wall functions in the near-wall region, the kinetic energy boundary condition calculated at the edge of the three dimensional domain is based on the relationship given in (4), in which μ_t and l are obtained using the near-wall van Driest expressions[30]. Both the unidimensional element techniques employed the (k–l) model in the near-wall region involving the solution of the kinetic energy transport equation. Kinetic energy profile comparisons are made in *Figures 11* and *12*. It is evident that, in common with other workers, there exists an underprediction of the near wall peaks downstream which has been attributed to the standard modelled form of the diffusion term in the k-equation (5).

It is again encouraging that the unidimensional element based solutions are closer to the experimental near-wall peaks compared to the log law based solution for a given turbulence model. Similarity is again apparent between the solutions obtained using the ARS and (k–ε) models (*Figure 12*). Away from the near-wall region the predictions obtained employing these

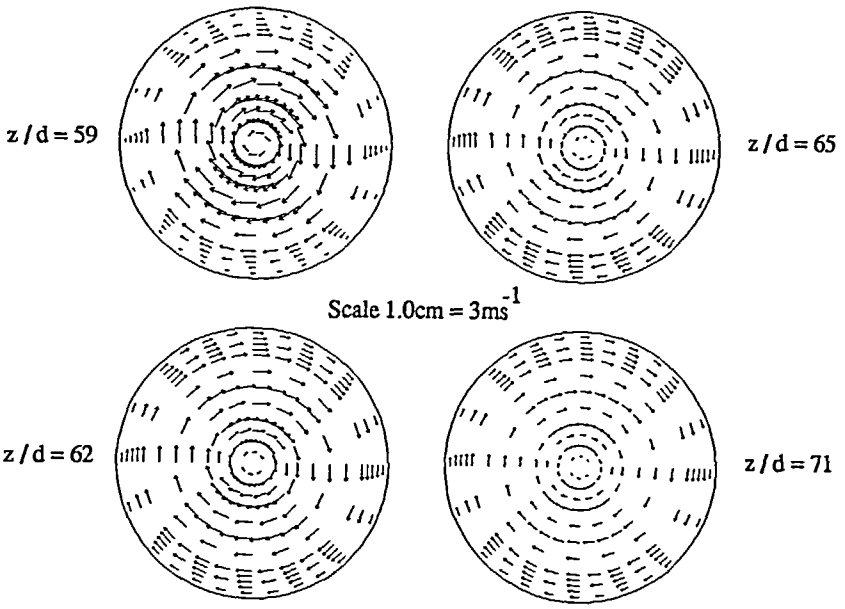

Figure 10 Predicted swirl velocity vectors (k–l) model and log laws

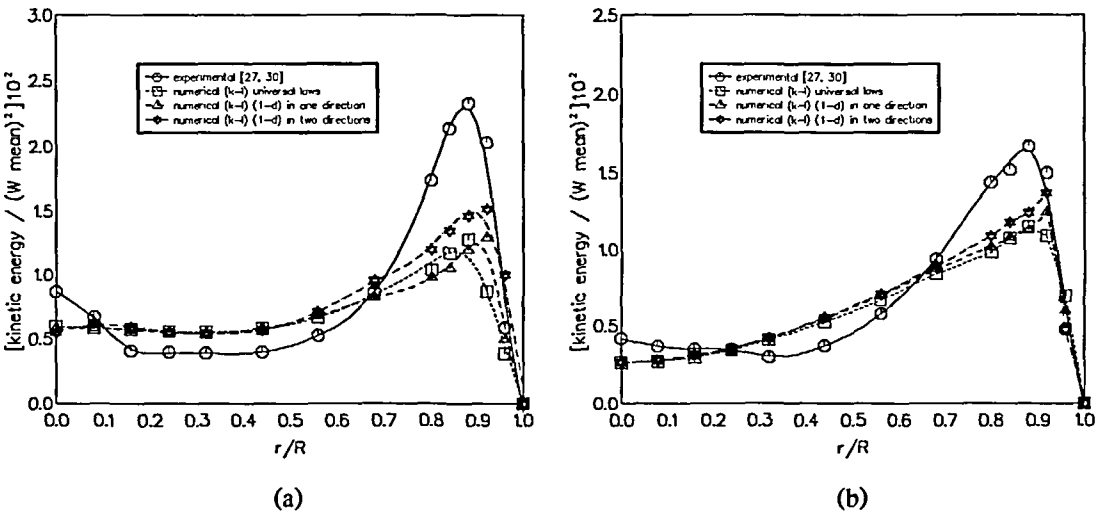

Figure 11 Kinetic energy comparison (k–l) model: (a) $z/d=62$; (b) $z/d=71$

turbulence models are closer to experiment than the (k–l) based solutions, which is to be expected due to the more realistic representation of the length scale.

Pressure drop comparisons are made in *Figure 13* of each of the numerical solutions with the experimental drop recorded between $z/d = 59$ and $z/d = 71$. The distributions are given relative to the pressure at $z/d = 59$ (P_o). All the models correctly predict a drop which is non-linear in form. The computed pressure field is closely linked to the approximation of the velocity field when solving the Navier–Stokes equations. The most satisfactory predictions of velocity, kinetic

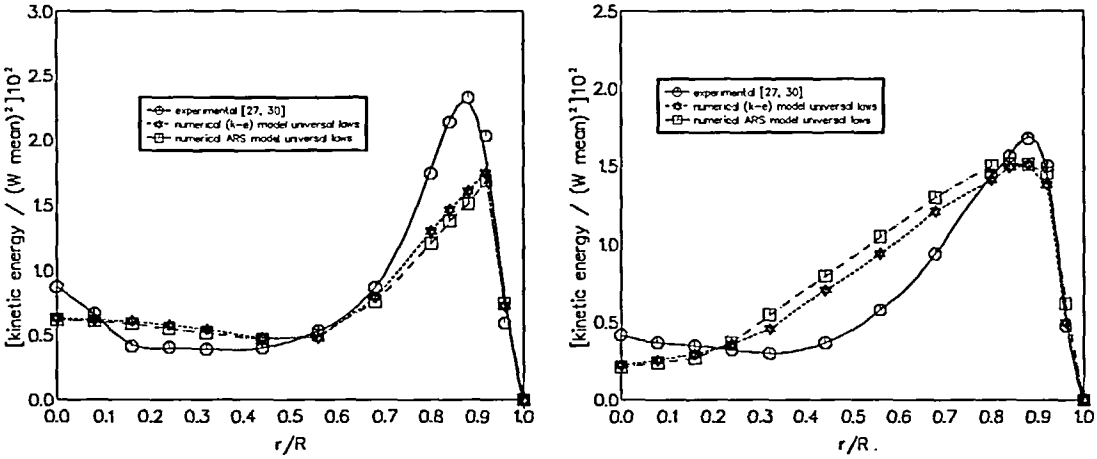

Figure 12 Kinetic energy comparisons (k–ε), ARS: (a) $z/d=62$; (b) $z/d=71$

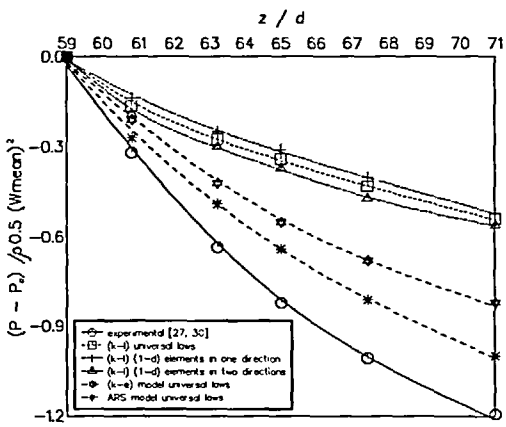

Figure 13 Numerical and experimental pressure drop comparison

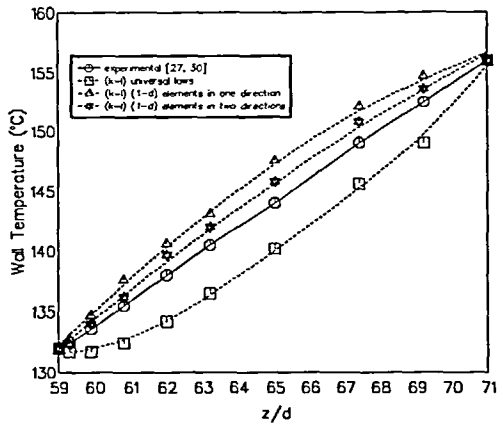

Figure 14 Comparison of experimental and numerical wall temperatures

energy and turbulent viscosity are likely to be consistent with the most satisfactory predicted pressure values. However, acceptable pressure distributions can sometimes be obtained when velocity gradients and stress components are inaccurate[18].

The one equation model values underestimate the pressure drop considerably (up to 60%), the distribution obtained through the use of the (1-d) elements in two directions shows a slight improvement relative to the use of wall functions. The previous differences in velocity and kinetic energy prediction between the (k–l) model and the higher order models, as a result of alternative representation of the length scale and the Reynolds stresses, are reflected in the differing pressure drop predictions. The most satisfactory predictions are obtained using the ARS model, the maximum difference from experiment downstream was approximately 18%.

When employing the solid/fluid model in the heat transfer problem an experimental uniform heat flux of 1.8 kW/m^2 was applied to the outer surface of the copper pipe. Temperature field predictions were calculated based on various isothermal solutions. As the predicted temperature

fields are dependent on the computed velocity and turbulent viscosity distributions, the heat transfer investigation is likely to highlight the differences in the isothermal solutions. In *Figure 14* a comparison is made between the predicted and experimental wall temperature distributions. Three numerical solutions are presented each based on flow solutions using varying near-wall techniques together with a (k–l) model of turbulence. All the resulting wall temperature predictions are to within 4% of the experimental values. It is evident that the improved isothermal solution employing (1-d) element strings in two directions in the near-wall region has resulted in improved prediction relative to the other methods.

The fluid bulk temperature predictions are also in satisfactory agreement with experiment, the comparisons having a maximum difference of $<2\%$, as shown in *Figure 15*. The numerical bulk temperature values at each of the axial locations downstream of the $z/d = 59$ position were calculated using the computed axial velocity values and air temperatures. The corresponding air temperature distributions computed at varying axial locations are given in the form of contour plots in *Figure 16*. Included in this Figure is the boundary condition at $z/d = 59$. The presence of the swirl at this position causes considerable temperature variation near the pipe wall indicated by the closeness of the contour lines in this region. Over the majority of this cross-section the air temperature varies little as indicated by the absence of contours. The heat transfer from the wall to the fluid is greater compared to flow without swirl at the same axial position.

The numerical model was found to satisfactorily agree with the experimental temperature variations downstream, differing by a maximum of 5% from experiment at all points downstream. The predicted temperature contours given in *Figure 16* correctly show a greater variation of air temperature across the pipe as the swirl decays downstream. The model has captured the reduction in the temperature gradient near the wall as the swirl decays, indicating a reduction in heat transfer. Finally heat transfer distributions along the section are given in the form of Nusselt numbers in *Figure 17*. In the current study the local Nusselt number is defined as:

$$Nu = \frac{q}{K_a} \frac{d}{\Delta T} \tag{20}$$

In *Figure 17*, the heat transfer rate is described in the form of a dimensionless ratio of the local Nusselt numbers associated with swirl and those associated with fully developed flow. It is seen that the experimental distribution comprises of ratios greater than unity. This indicates that the swirl present enhances the heat transfer rate relative to the fully developed value. All the numerical solutions obtained are to within 5% of the experimental data. It is again seen

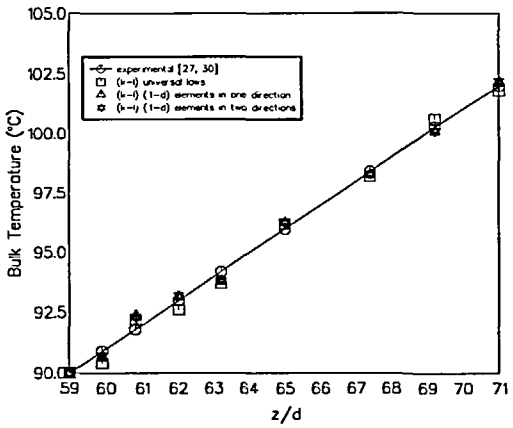

Figure 15 Comparison of experimental and numerical bulk temperatures

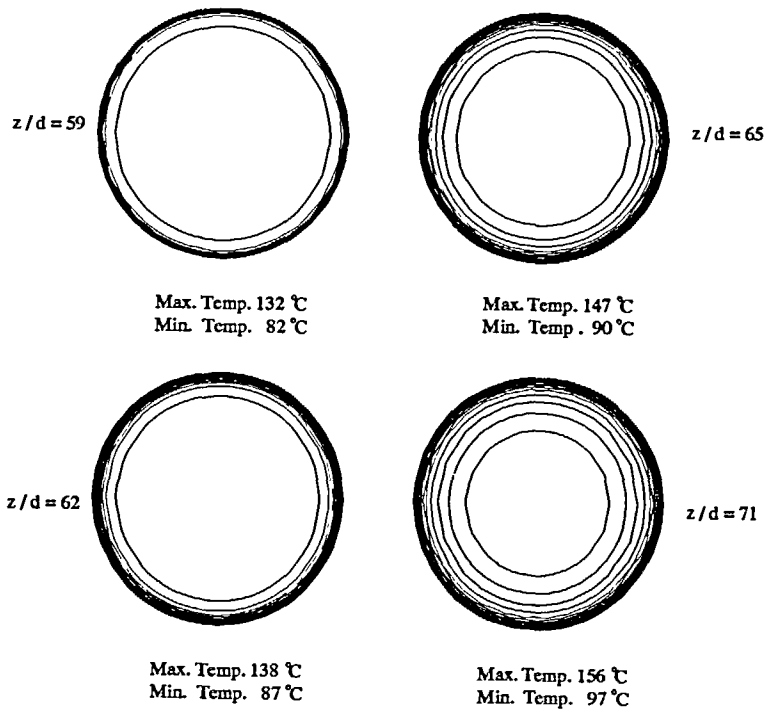

Figure 16 Predicted temperature contours (k–l) model and (1–d) elements

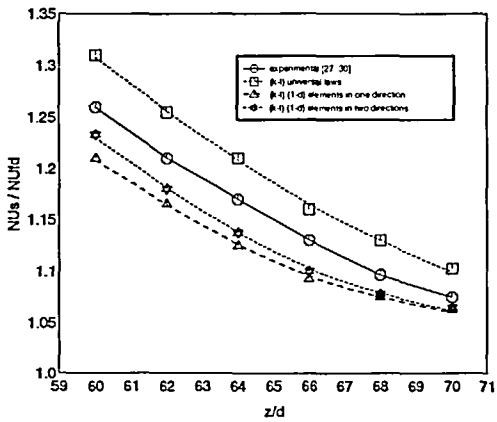

Figure 17 Comparison of experimental and numerical Nusselt numbers

that solutions based on flow predictions using the unidimensional element technique are closer to experiment compared to the log law based solution.

CONCLUSIONS

The current work represents one of the few finite element approaches of simulating decaying swirl in a pipe and, as far as the authors are aware, is the first to obtain satisfactory heat transfer

prediction by employing a finite element based solid/fluid model. From the relevant literature it would seem that even for relatively weakly swirling flow an entirely satisfactory prediction of the mean and turbulent quantities remains elusive. The advent of considerable computing power now enables workers to employ more comprehensive stress closures than previously employed but there is, clearly, considerable work necessary in order to implement them successfully in industry, particularly in a three-dimensional context.

From the present work it is evident that further work is necessary to predict such features as the correct movement of the swirl velocity maximum downstream and the size of the near-wall kinetic energy peaks. This work has deliberately avoided mesh dependency by employing a sufficiently fine mesh and sought to investigate alternative techniques of representing the underlying physical aspects of the problem such as the development of the unidimensional element technique. In common with previous work, this technique has lead to improved prediction which is highlighted in the heat transfer investigation.

Further work is necessary on the combination of the unidimensional element technique with each of the turbulence models employed. A parametric study would certainly be useful incorporating the techniques developed to model further published data. Future modelling of several flow rates, swirl strengths and varying heating conditions can perhaps establish a useful general formula for the heat transfer rate in decaying swirl in a pipe. A parametric study on the effect on predictions downstream by varying the upstream dissipation rate profile is also recommended. Even with reliable experimental data, the variation of the inlet dissipation rate distributions used in the relevant literature suggests that this is an area of uncertainty.

It is now widely acknowledged that the flexibility of the finite element method enables it to be applied successfully to a wide range of problems, often giving satisfactory prediction where other discretization techniques fail. Many workers now agree that the properties of the finite element method encourage its application and future development in the numerical simulation of swirling flows.

ACKNOWLEDGEMENTS

The authors would like to acknowledge the financial assistance of the Ministry of Defence and Rolls-Royce plc during this research.

REFERENCES

1 Gupta, A. K., Lilley, D. G. and Syred, N. *Swirl Flows*, Abacus Press, Tunbridge Wells (1984)
2 Gupta, A. K. and Lilley, D. G. *Flowfield Modeling and Diagnostics*, Abacus Press, Tunbridge Wells (1985)
3 Wheeler, R. W. Gasoline combustion past, present and future, in *Minutes of CI/CSS Spring Tech. Meet., Purdue University* (1978)
4 Heywood, J. B. Recent advances in combustion engineering, *Progr. Energy Combust. Sci.*, **1**, 135–165 (1976)
5 Morris, W. D. and Ayham, T. Observations on the influence of rotation on heat transfer in coolant channels of gas turbine blades, *Proc. Inst. Mech. Eng.*, **193** (21), 303–311 (1979)
6 Taylor, C., Xia, J. Y., Medwell, J. O. and Morris, W. D. Numerical simulation of three dimensional turbulent flow and heat transfer within a multi-ribbed cylindrical duct, *J. Fluid Mech.*, pp. 220–227 (1991)
7 Hogg, S. and Leschziner, M. A. Computation of highly swirling confined flow with a Reynolds stress turbulence model, *AIAA J.*, **27**, 57–63 (1989)
8 Khodadadi, J. M. and Vlachos, N. S. Computation of confined swirling flows: effects of boundary conditions and turbulence model, *Numerical Methods in Laminar and Turbulent Flow*, Pineridge Press, Swansea, pp. 458–469 (1987)
9 Benim, A. C. Finite element analysis of confined-turbulent swirling flows, *Int. J. Num. Meth. Fluids*, **11**, 697–717 (1990)
10 Abujelala, M. T. and Lilley, D. G. Limitations and empirical extensions of the k–ε model as applied to turbulent confined swirls, *Chem. Eng. Commun.*, **31**, 223–236 (1984)

11 Sloan, D. G., Smith, P. J. and Douglas Smoot, L. Modeling of swirl in turbulent flow systems, *Prog. Energy Combust. Sci.*, **12**, 163–250 (1986)
12 Chuang, S. H., Lin, H. C., Tai, F. M. and Sung, H. M. Hot flow analysis of swirling sudden-expansion dump combustor, *Int. J. Num. Meth. Fluids*, **14**, 217–239 (1992)
13 Armfield, S. W. and Fletcher, C. A. J. Comparison of k–ε and algebraic Reynolds stress models for swirling diffuser flow, *Int. J. Num. Meth. Fluids*, **9**, 987–1009 (1989)
14 Fu, S., Huang, P. G., Launder, B. E. and Leschziner, M. A. A comparison of algebraic and differential second-moment closures for axisymmetric turbulent shear flows with and without swirl, *J. Fluids Eng.*, **110**, 216–221 (1988)
15 Hutton, A. G., Smith, R. M. and Hickmott, S. The computation of turbulent flows of industrial complexity by the finite element method—progress and prospects, *Int. J. Num. Meth. Fluids*, **7**, 1277–1298 (1987)
16 Algifri, A. H. and Bhardwaj, R. K. Prediction of the heat transfer for decaying turbulent swirl flow in a tube, *Int. J. Heat Mass Transfer*, **28**, 1637–1642 (1984)
17 Huang, F. and Tsou, F. K. Friction and heat transfer in turbulent free swirling flow in pipes, *ASME Paper N79-HT-39* (1979)
18 Xia, J. Y., Taylor, C. and Medwell, J. O. Finite element modelling of the near wall zone of confined turbulent flows, *Eng. Comput.*, **6**, 127–132 (1989)
19 Boussinesq, J. Theorie de l'ecoulement tourbillonnant et tumultueux des liquides dans les lits rectilignes a grande section, *C. R. Acad. Sci.*, **123**, 1290–1295 (1897)
20 Taylor, C. and Morgan, K. *Computational Techniques in Transient and Turbulent Flow*, Pineridge Press, Swansea (1981)
21 Jones, W. P. and Launder, B. E. The prediction of laminarization with a two-equation model of turbulence, *Int. J. Heat Mass Transfer*, **15**, 301–314 (1972)
22 Thomas, C. Analysis of confined turbulent flow, *PhD Thesis*, University College of Swansea (1982)
23 Launder, B. E., Reece, G. J. and Rodi, W. Progress in the development of a Reynolds-stress turbulence closure, *J. Fluid Mech.*, **68**, 537–566 (1975)
24 Naot, D., Shavit, A. and Wolfshtein, M. Interactions between components of the turbulent velocity correlation tensor due to pressure fluctuations, *Israel J. Technol.*, **8**, 259–269 (1970)
25 Rotta, J. C. Turbulent boundary layers in incompressible flow, *Progr. Aerosp. Sci.*, **2**, (1962)
26 Demuren, A. O. and Rodi, W. Calculation of turbulence-driven secondary motion in non-circular ducts, *J. Fluid Mech.*, **140**, 189–222 (1984)
27 Chang, T. H. An investigation of turbulent swirling flow with heat transfer, *PhD Thesis*, University College of Swansea (1991)
28 Schlichting, H. *Boundary Layer Theory*, McGraw-Hill, New York (1968)
29 Sparrow, E. M. and Chaboki, A. Swirl-affected turbulent fluid flow and heat transfer in a circular tube, *J. Heat Transfer*, **106**, 766–773 (1984)
30 Casey, M. R. Heat transfer characterisation of three-dimensional turbulent flow with swirl, *PhD Thesis*, University College of Swansea (1992)
31 Zienkiewicz, O. C. *The Finite Element Method*, McGraw-Hill, New York (1977)
32 Weske, D. R. and Sturov, G. Y. Experimental study of turbulent swirled flows in a cylindrical tube, *Sov. Res. Fluid Mech.*, **3**, 77–82 (1974)

APPENDIX

Reynolds stress components

$$\overline{u_1'^2} = \frac{\dfrac{2k}{C_1\varepsilon}\left\{\dfrac{P_1}{3}(\alpha+\beta+C_1-1) - \overline{u_1'u_3'}\left[(1-\alpha)\dfrac{\partial\overline{u_1}}{\partial x_3} - \beta\dfrac{\partial\overline{u_3}}{\partial x_1}\right]\right\}}{1+\dfrac{2k}{C_1\varepsilon}(1-\alpha-\beta)\dfrac{\partial\overline{u_1}}{\partial x_1}} + \frac{\dfrac{2k}{C_1\varepsilon}\left\{-\overline{u_1'u_2'}\left[(1-\alpha)\dfrac{\partial\overline{u_1}}{\partial x_2} - \beta\dfrac{\partial\overline{u_2}}{\partial x_1}\right] - \gamma k\dfrac{\partial\overline{u_1}}{\partial x_1}\right\}}{1+\dfrac{2k}{C_1\varepsilon}(1-\alpha-\beta)\dfrac{\partial\overline{u_1}}{\partial x_1}} \quad (21)$$

$$\overline{u_2'^2} = \frac{\dfrac{2k}{C_1\varepsilon}\left\{\dfrac{P_2}{3}(\alpha+\beta+C_1-1) - \overline{u_2'u_3'}\left[(1-\alpha)\dfrac{\partial \overline{u_2}}{\partial x_3} - \beta\dfrac{\partial \overline{u_3}}{\partial x_2}\right]\right\}}{1+\dfrac{2k}{C_1\varepsilon}(1-\alpha-\beta)\dfrac{\partial \overline{u_2}}{\partial x_2}} + \frac{\dfrac{2k}{C_1\varepsilon}\left\{-\overline{u_2'u_1'}\left[(1-\alpha)\dfrac{\partial \overline{u_2}}{\partial x_1} - \beta\dfrac{\partial \overline{u_1}}{\partial x_2}\right] - \gamma k\dfrac{\partial \overline{u_2}}{\partial x_2}\right\}}{1+\dfrac{2k}{C_1\varepsilon}(1-\alpha-\beta)\dfrac{\partial \overline{u_2}}{\partial x_2}} \quad (22)$$

$$\overline{u_3'^2} = \frac{\dfrac{2k}{C_1\varepsilon}\left\{\dfrac{P_3}{3}(\alpha+\beta+C_1-1) - \overline{u_3'u_2'}\left[(1-\alpha)\dfrac{\partial \overline{u_3}}{\partial x_2} - \beta\dfrac{\partial \overline{u_2}}{\partial x_3}\right]\right\}}{1+\dfrac{2k}{C_1\varepsilon}(1-\alpha-\beta)\dfrac{\partial \overline{u_3}}{\partial x_3}} + \frac{\dfrac{2k}{C_1\varepsilon}\left\{-\overline{u_3'u_1'}\left[(1-\alpha)\dfrac{\partial \overline{u_3}}{\partial x_1} - \beta\dfrac{\partial \overline{u_1}}{\partial x_3}\right] - \gamma k\dfrac{\partial \overline{u_3}}{\partial x_3}\right\}}{1+\dfrac{2k}{C_1\varepsilon}(1-\alpha-\beta)\dfrac{\partial \overline{u_3}}{\partial x_3}} \quad (23)$$

$$\overline{u_2'u_3'} = \frac{\dfrac{k}{C_1\varepsilon}\left\{\beta\left[\overline{u_1'u_3'}\dfrac{\partial \overline{u_1}}{\partial x_2} + \overline{u_1'u_2'}\dfrac{\partial \overline{u_1}}{\partial x_3}\right] - [(1-\alpha)\overline{u_2'^2} - \beta\overline{u_3'^2} + \gamma k]\dfrac{\partial \overline{u_3}}{\partial x_2}\right\}}{1+\dfrac{k}{C_1\varepsilon}(1-\alpha-\beta)\left(\dfrac{\partial \overline{u_2}}{\partial x_2} + \dfrac{\partial \overline{u_3}}{\partial x_3}\right)} + \frac{\dfrac{k}{C_1\varepsilon}\left\{\left[-(1-\alpha)\left(\overline{u_1'u_2'}\dfrac{\partial \overline{u_3}}{\partial x_1} + \overline{u_1'u_3'}\dfrac{\partial \overline{u_2}}{\partial x_1}\right)\right] - [(1-\alpha)\overline{u_3'^2} - \beta\overline{u_2'^2} + \gamma k]\dfrac{\partial \overline{u_2}}{\partial x_3}\right\}}{1+\dfrac{k}{C_1\varepsilon}(1-\alpha-\beta)\left(\dfrac{\partial \overline{u_2}}{\partial x_2} + \dfrac{\partial \overline{u_3}}{\partial x_3}\right)} \quad (24)$$

$$\overline{u_1'u_2'} = \frac{\dfrac{k}{C_1\varepsilon}\left\{\beta\left[\overline{u_1'u_3'}\dfrac{\partial \overline{u_3}}{\partial x_2} + \overline{u_2'u_3'}\dfrac{\partial \overline{u_3}}{\partial x_1}\right] - [(1-\alpha)\overline{u_2'^2} - \beta\overline{u_1'^2} + \gamma k]\dfrac{\partial \overline{u_1}}{\partial x_2}\right\}}{1+\dfrac{k}{C_1\varepsilon}(1-\alpha-\beta)\left(\dfrac{\partial \overline{u_2}}{\partial x_2} + \dfrac{\partial \overline{u_1}}{\partial x_1}\right)} + \frac{\dfrac{k}{C_1\varepsilon}\left\{\left[-(1-\alpha)\left(\overline{u_2'u_3'}\dfrac{\partial \overline{u_1}}{\partial x_3} + \overline{u_1'u_3'}\dfrac{\partial \overline{u_2}}{\partial x_3}\right)\right] - [(1-\alpha)\overline{u_1'^2} - \beta\overline{u_2'^2} + \gamma k]\dfrac{\partial \overline{u_2}}{\partial x_1}\right\}}{1+\dfrac{k}{C_1\varepsilon}(1-\alpha-\beta)\left(\dfrac{\partial \overline{u_2}}{\partial x_2} + \dfrac{\partial \overline{u_1}}{\partial x_1}\right)} \quad (25)$$

$$\overline{u_1'u_3'} = \frac{\dfrac{k}{C_1\varepsilon}\left\{\beta\left[\overline{u_1'u_2'}\dfrac{\partial\overline{u_2}}{\partial x_3} + \overline{u_2'u_3'}\dfrac{\partial\overline{u_2}}{\partial x_1}\right] - [(1-\alpha)\overline{u_3'^2} - \beta\overline{u_1'^2} + \gamma k]\dfrac{\partial\overline{u_1}}{\partial x_3}\right\}}{1 + \dfrac{k}{C_1\varepsilon}(1-\alpha-\beta)\left(\dfrac{\partial\overline{u_3}}{\partial x_3} + \dfrac{\partial\overline{u_1}}{\partial x_1}\right)}$$
$$+ \frac{\dfrac{k}{C_1\varepsilon}\left\{\left[-(1-\alpha)\left(\overline{u_2'u_3'}\dfrac{\partial\overline{u_1}}{\partial x_2} + \overline{u_1'u_2'}\dfrac{\partial\overline{u_3}}{\partial x_2}\right)\right] - [(1-\alpha)\overline{u_1'^2} - \beta\overline{u_2'^2} + \gamma k]\dfrac{\partial\overline{u_3}}{\partial x_1}\right\}}{1 + \dfrac{k}{C_1\varepsilon}(1-\alpha-\beta)\left(\dfrac{\partial\overline{u_3}}{\partial x_3} + \dfrac{\partial\overline{u_1}}{\partial x_1}\right)} \tag{26}$$

where:

$$P_1 = \nu_t\left[2\left(\frac{\partial\overline{u_1}}{\partial x_1}\right)^2 + \left(\frac{\partial\overline{u_1}}{\partial x_2}\right)^2 + \left(\frac{\partial\overline{u_1}}{\partial x_3}\right)^2 + \frac{\partial\overline{u_2}}{\partial x_1}\frac{\partial\overline{u_1}}{\partial x_2} + \frac{\partial\overline{u_3}}{\partial x_1}\frac{\partial\overline{u_1}}{\partial x_3}\right]$$
$$P_2 = \nu_t\left[\left(\frac{\partial\overline{u_2}}{\partial x_1}\right)^2 + 2\left(\frac{\partial\overline{u_2}}{\partial x_2}\right)^2 + \left(\frac{\partial\overline{u_2}}{\partial x_3}\right)^2 + \frac{\partial\overline{u_1}}{\partial x_2}\frac{\partial\overline{u_2}}{\partial x_1} + \frac{\partial\overline{u_3}}{\partial x_2}\frac{\partial\overline{u_2}}{\partial x_3}\right]$$
$$P_3 = \nu_t\left[2\left(\frac{\partial\overline{u_3}}{\partial x_1}\right)^2 + \left(\frac{\partial\overline{u_3}}{\partial x_2}\right)^2 + \left(\frac{\partial\overline{u_3}}{\partial x_3}\right)^2 + \frac{\partial\overline{u_1}}{\partial x_3}\frac{\partial\overline{u_3}}{\partial x_1} + \frac{\partial\overline{u_2}}{\partial x_3}\frac{\partial\overline{u_3}}{\partial x_2}\right] \tag{27}$$